J. Fluid Mech. (1983), *vol.* 128, *pp.* 59–80
Printed in Great Britain

Internal mixing in stratified fluids

By A. D. McEWAN†
CSIRO Division of Atmospheric Physics, Aspendale, Victoria, Australia

(Received 24 June 1981 and in revised form 18 August 1982)

Using experimental measurements, estimates are made of the efficiency of conversion of kinetic energy into potential energy through vertical mixing in a continuously stratified fluid. In the experiments kinetic energy was supplied continuously at a rate of ϵ to a fundamental internal wave mode in a rectangularly bounded and initially linear stable stratification. Mixing resulted from the instability of this wave and its consequent 'breaking'. Potential energy was gained by the system at rate $\dot{p}$ through the gradual weakening of the stratification.

The instability is predictable using wave-interaction theory, affording a means of estimating the amount of kinetic energy lost (at rate ϵ_V) to laminar viscosity without first cascading to the fine scales characteristic of turbulent mixing.

With account taken of this viscous loss the mixing efficiency $\dot{p}/\epsilon_M$, based upon the residual kinetic energy input ϵ_M ($= \epsilon - \epsilon_V$) was found to be approximately constant, and not significantly correlated with the rate at which energy was supplied, nor with the estimated instantaneous minimum gradient Richardson number. The average value for eight separate experimental runs using two different experimental configurations was 0·26 with a sample standard deviation of 0·06.

Measured density profiles also afforded an estimate of the effective vertical diffusivity κ_d of density as a result of mixing. Vertically averaged values of the product of κ_d and the squared local static buoyancy frequency N, $\overline{\kappa_d N^2}$, were found to have an average for seven runs of $0{\cdot}24\epsilon_M$, with a standard deviation for the coefficient of 0·1, and no significant correlation with energy supply rate.

These results, the first of their kind to correct for incidental losses, substantiate the values previously assumed in estimates of dissipation and vertical diffusion in the ocean and the atmosphere, and validate the assumption of similarity between buoyancy and mass transfer on which they are based. The efficiency value also agrees with the kinematic prediction for localized homogenization in small discrete volumes made in the companion paper (McEwan 1983). On the basis of that work it is inferred from the present results that the mixing efficiency is only weakly dependent upon Prandtl number provided that this is of order unity or greater.

1. Introduction

Internal waves and wavelike instabilities lie at the small end of the spectrum of scales of motion in the atmosphere and the ocean. Although their energy density is low compared with the larger scales, they may be important because they could represent the primary conduit of energetic dissipation (Woods 1980), and, as such, one major factor defining the vertical diffusive properties of the medium.

Kinetic energy communicated to internal waves is lost through the occasional occurrence of intense finite-amplitude distortion. Such events cause 'breaking', the

† Present address: CSIRO Division of Oceanography, P.O. Box 21, Cronulla, N.S.W., Australia.

abrupt and irreversible creation of interleaved microstructure, which increases gradients to a degree where molecular diffusion will cause a significant macroscopic transfer of momentum and fluid properties during the lifetime of the event (McEwan 1983). The transfer of momentum involves a loss of kinetic energy, while the upward net transfer of density in a prevailing stable stratification represents an irreversible gain in the potential energy of the fluid mass. If $\dot{p}$ is the rate of acquisition of potential energy per unit fluid mass as a result of an energy flux ϵ into internal motions, within a stratification characterized by buoyancy frequency N, viscosity ν and molecular diffusivity of density κ_s, and the nature of the motion is definable in terms of dynamical scales, most particularly a vertical shear $\partial u/\partial z$, then

$$\frac{\dot{p}}{\epsilon} = R_f\left(\nu\kappa_s^{-1}, \nu N^2\epsilon^{-1}, \left(\frac{N}{\partial u/\partial z}\right)^2\right). \tag{1}$$

$\dot{p}/\epsilon$ is usually referred to as 'flux Richardson number' R_f, by virtue of an analogy drawn between buoyancy and momentum transfer in horizontal shearing motion (Turner 1973).

An assumption underpinning much of the theory and most of the experimental work on convective dynamics is that turbulent diffusion on macroscopic scales vastly exceeds molecular diffusion. If so, diffusivities might cease to be important and R_f would then depend only on Richardson number (the last dimensionless number in (1)) or some similar inertial parameter characterizing the overall motion. This is the kind of dependence implied in Linden's (1979) collation of stratified-mixing experiments, but should be regarded with caution in internally generated mixing, and oceanic mixing in particular. Cross-isopycnal mixing in the deep ocean is evidently small (Gregg & Briscoe 1979) because turbulent mixing events are disperse, infrequent, and limited in volume (Gargett 1976). Therefore while molecular diffusivity may be insignificant in the mixing events themselves, the internal dissipation rate ϵ averaged over the whole fluid volume may include a large component of laminar viscous dissipation which contributes nothing to the vertical mixing. Therefore in defining vertical diffusion and potential energy gain the appropriate scaling is the dissipation in mixing events, or for practical purposes (since it is virtually impossible to discriminate between mixing and non-mixing events on fine scales) the energy flux ϵ_M into mixing scales.

Providing the actively mixing volume is always small at any moment it seems justifiable to assume that this dissipation is independent of viscous dissipation on larger scales, ϵ_V, and so the total dissipation is written

$$\epsilon = \epsilon_V + \epsilon_M, \tag{2}$$

where ϵ_M *includes* viscous dissipation in mixing scales, which are presumed to be smaller than the resolvable scales of the disturbance motion, and at least as small as the buoyancy subscale $(\epsilon_M/N^3)^{\frac{1}{2}}$.

The significant question now is how does $\dot{p}$ in (1) depend on the other variables, and in particular does the ratio $\dot{p}/\epsilon_M$ (distinguished from flux Richardson number $\dot{p}/\epsilon$ by the title 'mixing efficiency' and designated η hereinafter) have properties generalizable in terms of these variables? For an answer, the difficulty with existing experimental results is that ϵ_V, although unavoidably a large component of ϵ on an experimental scale, has not been isolated in the measurements. This is reflected in the correlation suggested by Linden (1979), in which R_f, necessarily zero when stratification is absent (since all ϵ_M is expended in turbulent dissipation without buoyancy change), rises to a maximum then falls gradually as stability is increased.

This must be at least partly because ϵ_M/ϵ_V also decreases since mixing is less frequent or intense. A further difficulty is that most experiments relate to interfacial mixing between homogeneous layers. The mixing is, therefore, spatially variable in character, and possibly dependent in an unrealistic fashion on the forcing technique.

The present experiments were conceived in an attempt to minimize these difficulties. Internal waves bounded within a container in a continuous stratification can be well described by linear theory and, when forced to saturation, cascade their energy to resonantly interacting parasitic modes in an orderly and predictable fashion (McEwan, Mander & Smith 1972), leading to intermittent but widespread breaking and mixing. This allows ϵ_V to be estimated and separated from a measurable input power per unit mass ϵ. Periodic measurement of the stratification profile and integration of the one-dimensional diffusion equation using these measurements gives η and the profile of equivalent vertical diffusion coefficients $\kappa_d(z)$.

The experiments are described in §2. Section 3 outlines the calculation procedure, further details of which are given in the appendix. The results are given in §§4 and 5 and discussed in §6. This work accompanies a descriptive study of wave-induced internal mixing (McEwan 1983), which also includes predictions of mixing efficiency based on kinematical models of the mixing process. The results of these two studies are consistent and suggest an approximately constant efficiency of about $\frac{1}{4}$ for internal wave-inducing mixing.

2. Experiments

Experiments were made using a rectangular plate-glass tank 22·8 cm wide, 30 cm deep and 62 cm long, filled to the requisite level by a linearly stratified salt solution. Two wave-forcing configurations were used. In the first, (*a*) (figure 1*a*), a plane paddle was suspended by a trunnion frame near one end of the tank to enclose a water volume of 50·0 cm length. The paddle pivoted about a midplane horizontal axis, and was sealed around its edges against the sides of the glass tank by flaps made of felt. The face of the paddle was recessed, and into this recess there fitted an inner paddle which cleared the edges of the recess with a gap of between 0·7 and 1·3 mm. The space between the back of the inner paddle and the face of the recess was about 3·0 mm, and the face of both paddles was coplanar and vertical in the mean position. The inner paddle pivoted coaxially with the outer paddle pivots on delicate and frictionless steel flexure pivots. When the tank was properly filled, polystyrene sheets were floated on the surface to provide a rigid and non-diffusing upper surface.

Mounted centrally above water level on the face of the outer paddle was a sensitive ($\pm 0{\cdot}25$ N) semiconductor force transducer, connecting by cotton threads to a yoke on the inner paddle so that it could be used to measure the net moment μ acting on the inner paddle. The outer paddle was connected, via a triangular frame, to a variable-stroke scotch yoke driven by an electronically controlled stepping motor. The yoke displacement and hence paddle rotation $\alpha(t)$ was measured by an induction-type displacement transducer.

The output of both transducers was fed directly to a pen recorder and to an on-line computer programmed to calculate and return via teleprinter the work done per cycle of oscillation $\int \mu d\alpha$ on the inner paddle, and to record a running total of this work.

Because the inner paddle was 1·5 cm narrower than the tank and did not extend the full fluid depth, it was necessary to correct the work input calculated by this integration. Since the correction factor was sensitive to the detailed stratification profile, and because of the indeterminable effects of leakage past both paddles, a series

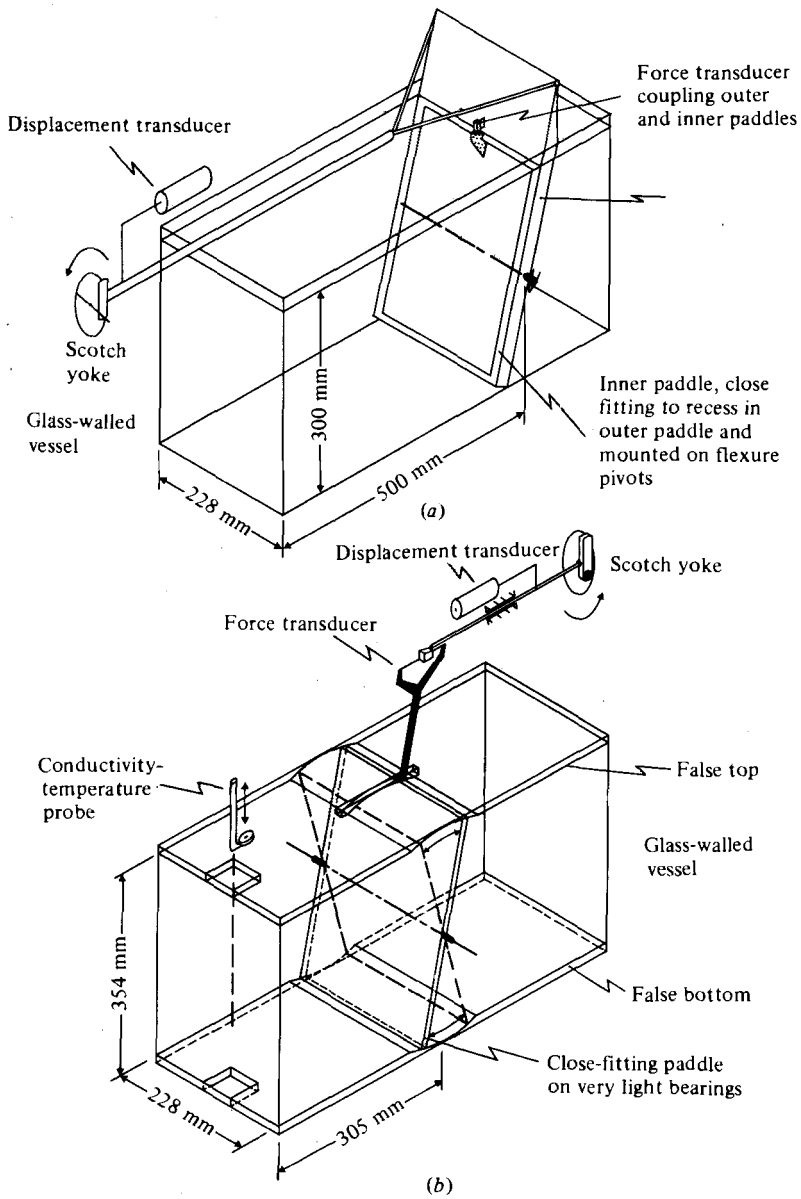

FIGURE 1. Experimental configurations.

of experiments were made with the second configuration (*b*). For this (figure 1*b*) a dismountable paddle was made which swung on very light ball bearings about a horizontal and accurately central lateral axis. This paddle was carefully made to clear the sides of the tank with a gap on each side of one millimetre. A false bottom 10 mm deep was fitted and provided with a recess to accommodate the swing of the paddle with a clearance of one millimetre. A false top similarly recessed and with a slot for an arm on the paddle was also fitted. Both the top and bottom had removable cutouts for a salinity probe.

In this configuration the force transducer was mounted directly on to the scotch-yoke piston, and was linked to an extension yoke on the paddle by tensioned threads.

In both configurations the fluid column was sounded between runs by a conductivity temperature probe, comprising a thermistor and a four-electrode conductivity element, calibrated and checked between soundings in prepared saline solutions. Data from downward and upward soundings were logged and used to calculate numerically the net centre of gravity of the fluid column, and the resonance conditions for the internal wave modes.

To observe the internal motions, a 30 cm schlieren system was used in which variations in the vertical refractive index gradient were visualized and photographed in grades of colour.

The experimental procedure was first to set up (by the two-tank method) a salinity stratification, ranging in density between 1·004 and 1·05 g/cm^3. For a frequency appropriate to resonance of the fundamental standing internal wave mode (half a wavelength in both horizontal and vertical) the paddle oscillation amplitude was then increased in small stages from a small level to that for which wave-interaction instability was clearly present. For each stage the steady-state wave amplitude, as indicated by neutrally buoyant beads in suspension, together with the paddle moment and frequency and amplitude decay rate on cessation of forcing were recorded, affording a means of calibrating the paddle moment measurement against wave amplitude (and net kinetic energy) and estimating the net viscous-damping coefficient of the fundamental mode, including damping due to leakage around the paddle and the false top.

The quiescent water column was sounded again, then the paddle amplitude was increased and sustained at a level where breaking of the forced wave could be seen to occur. Forcing frequency was adjusted to sustain at the highest level the energy input per cycles of oscillation as computed for each successive cycle and returned to the laboratory by teleprinter.

After several hundred cycles, the forcing was stopped with the paddle in mid-position and the wave was allowed to decay. Another sounding was taken; then the process was repeated with forcing at successively higher levels.

3. Calculation procedure

Since dissipation not associated with mixing represents a large proportion of the total energy input in any experiment of laboratory scale, the success of the present experiment depended heavily on estimating this dissipation accurately. Accordingly the form and amplitude of the wavelike motion from which it derived needed accurate description.

The basis of calculation was the evident simplicity and predictability of wave modes and cascades in a rectangular bounded system.

The main component of the dissipation was that due to the forced mode itself, whose amplitude was directly measurable. In planning the experiment it was hoped that losses to the higher modes could also be found directly by the measurement of amplitude decay after the cessation of forcing but this was not so, and it became necessary to find these losses by calculation. The procedure used is outlined below.

3.1. *Potential-energy gain*

The net energy gained by the system was determined from the increase in elevation of the centre of gravity δz^* of the static fluid column before and after each mixing run as determined from density soundings. Results were corrected for the hysteresis between upward and downward soundings due to wake effects on the probe

(notwithstanding a sounding speed of 1 mm/s) and possible drift in the calibration of absolute density, by imposing mass conservation on the density and centre-of-gravity integrations.

3.2. *Dominant waves and their amplitudes*

Above a critical amplitude, the forced-wave mode (a standing wave of half-wavelength equal to the boundary dimensions in vertical and horizontal) loses energy by resonantly interactive cascade to identifiable higher modes of lower frequencies, whose amplitudes can be calculated providing their own rate of dissipation is known. This was demonstrated for single cascades by McEwan *et al.* (1972), and the calculation was extended here to double cascades, where the higher modes are themselves potentially unstable (see the appendix).

The dominant cascade modes could be identified with a degree of ambiguity from the schlieren photographs and, in some cases, from the modulations of the measured paddle moment maxima, but a knowledge of component frequencies and amplitudes was still necessary. Resonant triad closure requires that frequencies of the parasites added together equal that of the forcing wave ((A 3) in the appendix). Commonly there exist many combinations of waves which meet this condition approximately.

The natural frequency of all the possible low-order wave modes was computed for the density profiles measured at the beginning and end of each run using (A 2) (in the appendix). This enabled the detuning effect on the interaction equations to be evaluated for all triads using the theory of McEwan & Plumb (1977).

For the determination of interaction and damping coefficients the simple linear field description for standing internal waves was assumed, i.e. (A 1)

$$\psi_j = A_j \sin\frac{M\pi}{h} z \sin\frac{K\pi}{l} x \sin\omega_j t \tag{3}$$

for modes j with modal numbers K and M, and frequencies ω_j for resonant closure determined as outlined in the appendix. Interaction and damping coefficients and forcing and moment relations were calculations using expressions given by McEwan (1971), (A 9) and (A 10). The damping coefficients combine dissipation in both the sidewall boundary Stokes layers, for which laminar viscosity alone (ν) was assumed and dissipation through *internal* strain alone, which assumed pseudo-viscosity ν_i whose magnitude required determination.

Using the interaction equations ((A 5), (A 6) *et seq.*), steady-state amplitudes of all the modes for each possible triad combination were computed, with the input forcing to the fundamental ($K = M = 1$) mode as defined by paddle oscillation amplitude. The mean fundamental mode amplitude was obtained from measured mean moment extrema on the paddle, calibrated over a range of wave amplitudes below those necessary for interactive instability against direct measurements of amplitude determined by excursions of centrally buoyant particles in the wave field. This made unnecessary a less reliable calculation based on the measured static density profile.

With the internal pseudo-viscosity as a parameter an iterative cycle was performed to equate the input net power to the net total dissipation in the fundamental mode plus the six lowest cascade modes,† as defined by their respective amplitudes and

† This number is the practical limit for unambiguity; the tertiary modes were usually well below the critical amplitude level predicted by linear theory using laminar viscosity.

dissipation coefficients. This is equivalent to making

$$F|\kappa|_a^2 A_a = \sum_a^g R_j(\nu_i)\,|\kappa|_j^2 A_j^2(\nu_i), \tag{4}$$

with terms as defined in the appendix.

The quantity $F|\kappa|_a^2 A_a = E$ is directly proportional to the total net power input per unit mass supplied to the forced mode, and is therefore proportional in a statistically steady system to ϵ, the net internal dissipation in this and smaller scales. F is a forcing function determined by the paddle amplitude and fundamental wave amplitude (q.v. (A 5)). Since this was not always steady during the course of an experimental run, the r.m.s. amplitude $\langle A_a \rangle$ of this wave was adopted in (4). $R_j(\nu_i)$ are the damping coefficients of modes j with the internal viscosity ν_i as a parameter.

3.3. *Energy partition and mixing efficiency*

With the amplitudes calculated as above so that (4) is satisfied, the power dissipated against laminar viscosity (V) in the boundary layers and the interior was calculated. With the same constant of proportionality as in (4),

$$V = \sum_a^g R_j(\nu)\,|\kappa|_j^2 A_j^2(\nu_i), \tag{5}$$

where $R_j(\nu)$ is the damping coefficient as given by (A 10) for each mode assuming only a laminar viscosity, i.e. $\nu_i = \nu$. V is thus equivalent to ϵ_V in (2). The quantity $(E-V)/E$ then defines an upper limit to the ratio ϵ_M/ϵ.

It is important to note the unavoidable assumptions implicit in the above operation, namely:

(*a*) that viscous and turbulent (or sub-wavescale) dissipation processes act independently upon the wave field;

(*b*) that the mixing energy descends directly into scales that are Fickian in their diffusion characteristics so far as their action in dissipating the wave energy is concerned, are isotropic and spatially uniform on average;

(*c*) that irreversible mass transfer occurs on the same scales as those receiving the mixing kinetic energy;

(*d*) none of the energy returns to wave kinetic energy by reverse energy cascade.

Finally the mixing efficiency was calculated as the ratio of the potential energy gained over the observed period during the run from the commencement of breaking activity to termination of forcing, to the total energy input P during that period, i.e.

$$\eta = \frac{Q\delta z^*}{P}\frac{E}{E-V}, \tag{6}$$

where Q is the total fluid mass in the wave-forcing region.

The calculation was repeated for all cascade possibilities compatible with observed moment modulations and/or schlieren-mode identification, as mentioned in (*a*) above.

3.4. *Gradient Richardson number*

As a basis for comparison in defining the degree of destabilization of the wave motion, a gradient Richardson number based on the sum of the maximum horizontal shear

magnitudes of each of the component waves was also calculated, i.e.

$$R_i = \frac{N^2}{\left(\sum_a^g A_j (M\pi/h)^2\right)^2}, \tag{7}$$

with terms defined in the appendix.

3.5. *Vertical diffusion*

If the one-dimensional diffusion equation

$$\frac{\partial \rho}{\partial t} = \frac{\partial}{\partial z}\left(\kappa_d \frac{\partial \rho}{\partial z}\right) \tag{8}$$

is adopted, the average vertical diffusivity of density $\kappa_d(z)$ can be computed for each run from successive soundings as a function of depth. Recorded density–depth sequences were first fitted by cubic splines in order that smooth derivatives $\partial\rho/\partial z$ could be obtained. Integration of (8) was then advanced from the position $z = a$ where $\partial\rho/\partial z$ (averaged over the time interval) was zero, whence $\kappa_d(a) = \Delta\rho(\partial^2\rho/\partial z^2)^{-1}\Delta t^{-1}$, where $\Delta\rho$ and Δt are density and time intervals between successive soundings. N^2 was computed concomitantly as a function of z to give a distribution of the product $\kappa_d N^2$ for comparison with ϵ and ϵ_M.

3.6. *Accuracy*

3.6.1. *Potential-energy gain.* Probe hysteresis and relocation errors were minimized by the imposition of mass conservation on the density and moment integration used in calculation of centre of gravity. The accuracy is thus estimated as that defined by the resolution of the density measurements ($\pm 10^{-4}$) amounting to $\pm 6 \times 10^{-4}$ cm in centre-of-gravity location. No allowance was made for leakage around the forcing paddle in the earlier configuration giving rise to a possible underestimation of several per cent in potential energy gained; however, the lack of a consistent negative anomaly between configurations (*a*) and (*b*) results suggest that no serious errors arose from this source.

3.6.2. *Kinetic-energy input.* Frequent recalibrations ensured that direct measurements of moment and amplitude were accurate to a fraction of a per cent, and comparison between calculated and observed moment–amplitude relations for non-breaking waves (see §5) confirmed that for configuration (*b*) the linear field description was adequate to better than 5 % in defining the motion up to breaking; the accuracy with configuration (*a*) was impaired by unmeasured moment contributions at the top and bottom of the paddle, and errors may have been as high as ± 10 %. The expression (6) used for the computation of η was intended to minimize errors from this source, by combining the measured energy inputs and gains with a total input/breaking energy fraction $E/(E-V)$ derived using calculated amplitudes. Thus the error is roughly the sum of centre-of-gravity errors plus an error arising from the error in the residue $E-V$ which depends in a complicated way on A_a. Taking the extremal values of all quantities yielded a ratio of about 0·45 between the lowest and highest estimates of η in most cases, and not less than 0·39. This range is equivalent to a range of 0·10 about the mean η found from the result, or 1·7 standard deviations.

4. Visual observations

After forcing commenced in each run, no significant mixing occurred before substantial interactive instability had developed. Usually the first modes to appear in the schlieren visualization, apart from the forced fundamental wave, were high in vertical wavenumber (M up to 30), and indicative (from their location near to the centre of the chamber) of parametric instability (see McEwan & Robinson 1975). Breaking first tended to occur in the same location, but spread throughout the interior within about 20 cycles of the forced mode. As breaking events and their residual fine structure became well distributed, there was a notable reduction in the wavenumber of the dominant parasitic modes, the final vertical mode number usually being between four and seven. This reflects the increased internal damping caused by the breaking, as a consequence of which the critical amplitude for unstable energization of the higher modal numbers is raised relative to that for the lower modes. The lower modes also become less sensitive to detuning from resonance (*q.v.* (A 7)). With the double-chamber configuration (figure 1 *b*) the motions on the opposite sides of the paddle retained a remarkable similarity in mode structure and even in the coincidence of breaking events throughout the duration of the whole experiment.

Typical schlieren images during breaking are reproduced in figure 2. The originals were colour transparencies, so some resolution and much interpretative material is lost in black and white. The reader is referred to the companion paper (McEwan 1983) for colour reproductions of a closely similar visualization and a detailed description of the breaking process.

The initial small scale of the unstable wave modulation is clearly evident in figure 2 (*a*) taken about 2 cycles after breaking was first observed. The inset shows the part of the field under observation. The forcing paddle is on the right. Both this figure and figure 2 (*b*) are retouched to emphasize the scaling bar of 20 cm total length, and to reveal regions of static instability ($\partial\rho/\partial z > 0$) in white hatching. The lightest colour defines zones where the density gradient is close to the static value, and regions of strongly enhanced density gradient (1·5 times the static gradient or greater) are delineated in white.

Figure 2 (*b*), taken after breaking has continued for some time at a somewhat larger forcing amplitude than 2 (*a*), shows that the wavenumber of the modulating disturbance is lower, and that a substantial part of the volume shows the grainy appearance indicative of mixing microstructure.

From this apparent chaos, three points are worthy of attention. First, the unstable regions are comparatively laminar in appearance, and even in a state of saturated forcing occupy a small proportion of the total volume. Mixing is subsequent to the formation of an unstable region, and not to any appreciable extent simultaneous with its presence. Secondly, the gradient of refractive index in the granulated regions, averaged along the light path, is weakened but not substantially different from the undisturbed static gradient. There is nothing to support the assumption common in previous speculations on the mechanics of breaking and mixing that there is an annihilation of the density gradient throughout the disturbed region. Thirdly, the residual effect of an accumulation of mixing events is a fine vertical modulation of the density gradient, with thin regions (in the present case, about 1 mm thick) of weakened density gradient bounded by thicker regions of slightly strengthened gradient. There was no evidence of strongly intensified gradients indicative of 'steppy' density microstructure. Together these support the conceptual correctness of McEwan's (1983) kinematic model and indicate that the irreversible mixing in

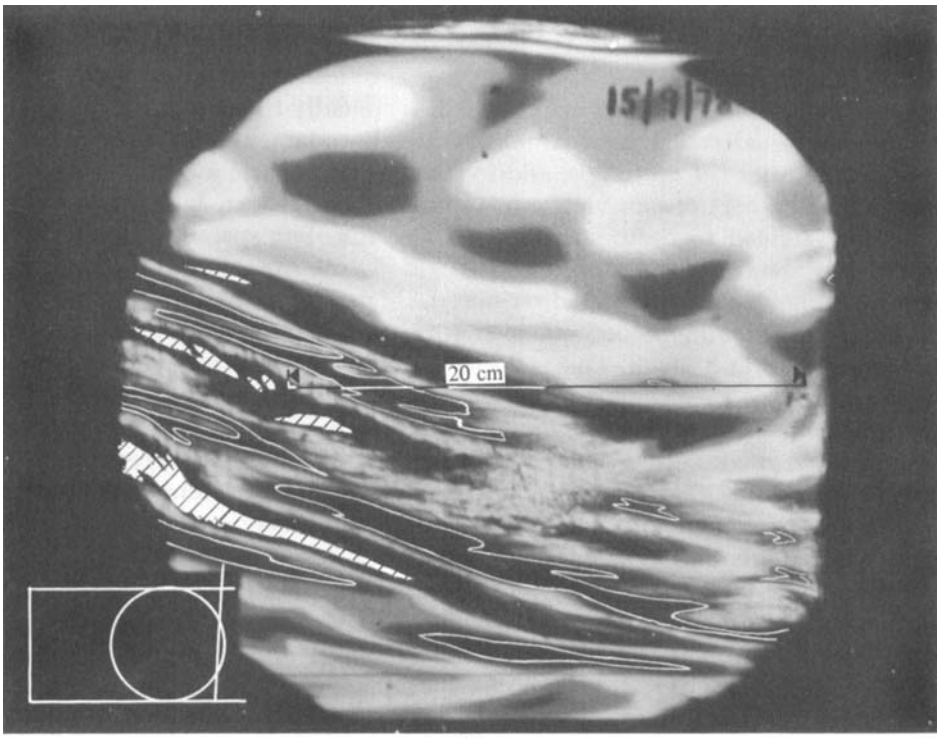

(*a*)

(*b*)

individual breaking events, even though widespread and intense, involves only a small proportion of the mixing volume.

5. Measurements

The first occurrence of breaking as shown by the paddle-moment measurement was an abrupt decrease in primary-moment amplitude, and an increase in resonant frequency. Although the procedure was to monitor the phase relation between paddle oscillation and moment continuously to maintain resonance, the amplitude tended to rise and fall as the intensity of the internal mixing declined following a mixing event, parasitic wave modes re-intensified, and breaking recurred.

Figure 3 shows the development in paddle-moment maximum over the full experimental range of forcing amplitudes in one experimental sequence. For the low level the steady-state moment has been plotted, while, for the unstable and breaking experiments, both the initial maximum attained before the complete development of instability and the final mean level with continuous sustained forcing are given. The forcing level at which fine modes first made their appearance, R, and the level for the first occurrence of significant breaking, B, are indicated. The theoretically predicted critical amplitude for the fundamental mode at which interactive instability is predicted under the conditions of column 6 (table 1), expressed as a moment maximum, is marked 'I'. The main predictions of interaction theory are borne out. In particular, the mean moment settles after R to the predicted critical fundamental amplitude level, then rises after B as internal dissipation increases.

Of seven experimental sequences, four were aborted or discarded due to technical or calibration problems. Table 1 summarizes the remaining three of the results, designated by the letters in the first row. For all runs the average value of N was about 1 s^{-1}.

The forcing function, row 2, defines the gross energy input rate per unit mass during the period of sustained wavebreaking, which is expressed as a dissipation rate in row 5. Rows 3 and 4 compare the measured fundamental mode amplitudes with that predicted by interaction theory, using the effective internal viscosity ν_i. The latter is always lower, implying that the internal damping is overestimated, and the proneness to tertiary instability is underestimated. The consequences of this are discussed later.

The potential energy gain rate over the period when breaking was observed is given in row 6 and the fraction that this represents of the input rate, which defines the conventional flux Richardson number, is listed in row 7.

The wave modes receiving the first cascade of input energy, row 8, have a bearing in determining the effective internal viscosity ν_i for closure of the energy-balance

---

FIGURE 2. Schlieren visualizations during breaking. Inset shows the part of the experimental tank in view. The paddle is on the right. These figures are reproduced from colour transparencies and are retouched to delineate regions of static instability in hatching on white, and regions where the local stable gradient of density is 1·5 times the static value by a white boundary. Lightest shades are regions of gradient close to the static value. (*a*) Two forcing cycles after breaking has commenced. A localized patch of mixed fluid from the first event lies beneath the scaling bar. The fine scale of the secondary wave structure is indicative of parametric instability. (*b*) After sustained breaking. The secondary wave structure is low in wavenumber and not clearly defined. Fine-scale layering density microstructure occupies most of the field, and breaking has occurred most recently near the bottom of the picture.

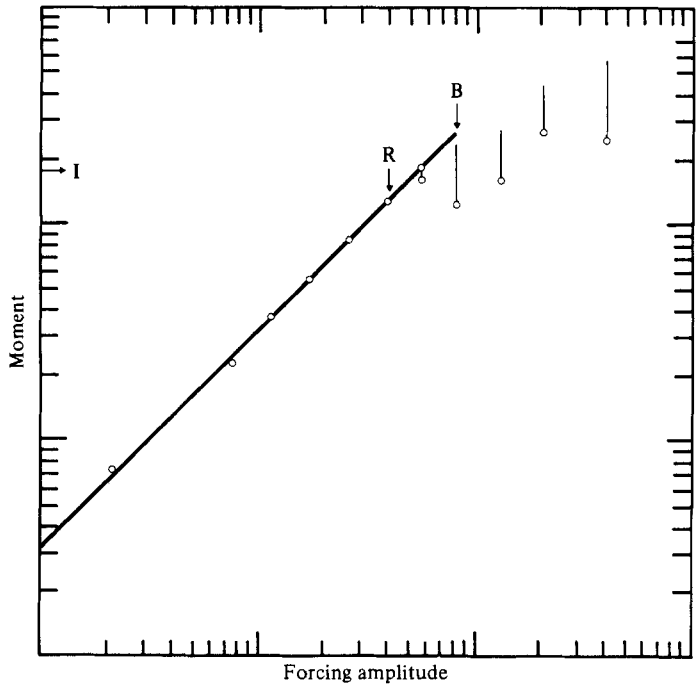

FIGURE 3. Paddle moment amplitude versus paddle displacement amplitude. ——, linear theory; ○, experimental values of equilibrium measured moment. Bars define the range of moment decrease following the first occurrence of instability. Level 'I' defines the predicted level for primary resonantly interactive instability. 'R' marks the first observed instability and 'B' is the first level at which 'breaking' and turbulence was evident.

equation (4) (expressed as proportion of laminar viscosity ν in row 10) and in defining the minimum gradient Richardson number (7) for the wave motion, row 15. The latter is strongly dependent upon the presence of tertiary modes (row 9) as reflected in the high values obtained for configuration (*b*), which was less disposed to instability.

Mixing-energy dissipation rate (row 11) determined from $E-V$ in (4) and (5) gives the net mixing efficiency η tabulated in row 12. The vertical diffusion rate found by integration of (8) over the period of observed breaking was corrected for molecular diffusion occurring during the interval between soundings. The product of diffusivity and local buoyancy frequency squared varied with depth. A representative profile is shown in figure 4.

Vertically averaged values are tabulated in row 13 and expressed as a fraction of ϵ_M in row 14. In one run a mechanically caused modulation on the density sounding made calculation inaccurate, and this result is deleted.

Row 16 lists the viscosity function in (1), using the vertically averaged value of N^2.

6. Discussion

6.1. *Flux Richardson number and mixing efficiency*

In this work a distinction is made between *flux Richardson number* $R_f \equiv \dot{p}/\epsilon$ and *mixing efficiency* $\eta = \dot{p}/\epsilon_M$. This is to reflect the possibility that on laboratory scales or for very intermittent mixing in the ocean or atmosphere a large component of ϵ is laminar viscous dissipation ϵ_V, which has no effect on the stratification.

For the purpose of calculation it has been necessary here to assume that the finest scales on which viscosity acts are those of calculable tertiary instabilities, which in reality cannot represent the finest scales on which motion proceeds without turbulent mixing. ϵ_M, being found as a residual $\epsilon - \epsilon_V$, is therefore probably overestimated, but by an amount depending in an obscure way upon the nature of the high-order wave cascade.

Table 1 shows that for the present experiments R_f was usually small compared with η because the viscous loss component of ϵ was large, even for intense mixing. Much of the loss was in wall friction, an inescapable component in any modestly scaled laboratory experiment.

For other laboratory experiments the 'non-mixing' component of the dissipation would be similarly large. In figure 5 both R_f and η are plotted against minimum gradient Richardson number R_i, together with the data presented by Linden (1979).

While the relevance of R_i as a dynamical parameter can be questioned in mixing induced as in the present case by short waves and without evidence of horizontal shearing instability, there is in common with the other experiments a slight negative correlation between R_f and R_i, in the range considered. From table 1 the variation coefficient is large and R_f is significantly correlated with ϵ. Since ν and N^2 were relatively constant there is a concomitant positive correlation with $\nu\overline{N^2}/\epsilon$.

In contrast the estimated average value of η was 0·26, comparable with the maximum R_f for shear induced intense interfacial mixing reported by Thorpe (1973) and Koop (1976). The coefficient of variance is about one quarter of that for R_f and the results yield no significant correlation with either R_i or $\nu\overline{N^2}/\epsilon$ over the widest achievable range of forcing conditions.

These results are consistent with the kinematical description of internal mixing given in McEwan (1983), which implies an insensitivity to input energy since mixing is seen as a series of widespread but volumetrically small events whose number density is determined by the rate of energization but having a similar evolution. Indeed the average obtained corresponds well with the value of $\frac{1}{4}$ derivable from that description on the assumption of intense and discrete mixing as well as with other estimates (e.g. Thompson 1980).

It also agrees conveniently with the value frequently assumed in mixing calculations (e.g. Olbers 1976; Lilley, Waco & Adelfang 1974).

6.2. *Vertical diffusivity*

Both dimensional and physical arguments indicate (*q.v.* Weinstock 1978) that, providing final viscous dissipation occurs on scales much smaller than those for vertical transport, the vertical diffusivity of buoyancy κ_d is defined by a single parameter $\kappa_d N^2/\epsilon_M$. The magnitude of this ratio is subject to debate, but the assumption of similarity permits a simple estimate in the case of turbulence generated by horizontal shear. In this case the rate of gain of potential energy through vertical turbulence flux of buoyancy is $\overline{gw'\rho'}/\rho$, where primes here denote turbulent variations from the mean, while the rate of working by the mean flow against Reynolds stress is $\overline{u'w'}\partial u/\partial z$.

In the present context the former term is equivalent to $\dot{p}$ and the latter to ϵ_M, since the viscous ϵ_V here concerns losses on scales larger than the mixing structures. Therefore since $N^2 = -g\rho^{-1}d\rho/dz$ and if vertical diffusivity is defined by a mean gradient of density, i.e. $\kappa_d = \overline{w'\rho'}(d\rho/dz)^{-1}$, substitution gives

$$\kappa_d = \eta\epsilon_M/N^2. \tag{9}$$

1 Configuration (figure 1)		† *a*		*a*			*b*			
2 Forcing function	F (cm^2 s^{-2})	0·38	0·61	0·46	0·58	0·75	0·38	0·57	0·89	
3 Measured mean amplitude	A_a (cm^2 s^{-1})	35·8	39·5	35·1	38·8	51·4	27·6	30·7	30·8	
4 Predicted critical amplitude	A_{ac} (cm^2 s^{-1})	35·9	47·7	39·2	44·3	62·7	31·0	34·7	35·0	
5 Input energy flux during wavebreaking	ϵ (cm^2 s^{-3} × 10^3)	43·8	78·1	48·0	70·5	125·3	48·3	81·4	126·5	
6 Potential-energy gain rate per unit mass	p (cm^2 s^{-3} × 10^3)	0·75	3·09	1·44	2·87	6·37	2·17	3·93	13·66	
7 Net flux Richardson number	$R_f = \frac{\dot{p}}{\epsilon}$	0·017	0·040	0·030	0·041	0·051	0·045	0·048	0·108	Average (sample standard deviation) 0·048 (0·027)
8 Identified primary destabilizing modes		1/4 2/3	1/4 2/3	3/7 4/8	1/4 2/3	1/4 2/3	2/6 3/7	1/4 2/5	1/4 2/5	
9 Tertiary modes also unstable?		Yes	Yes	Yes	Yes	Yes	No	No	No	
10 Effective internal viscosity	$\frac{\nu_i}{\nu}$	3·55	6·22	2·42	3·40	10·53	6·41	19·5	23·3	

11	Mixing-energy dissipation rate	ϵ_M (cm^2 s^{-3} $\times 10^3$)	2·7	11·8	4·5	11·7	17·6	8·2	26·5	65·7	Average (sample standard deviation) 0·26 (0·064)
12	Mixing efficiency	$\eta = \frac{\dot{p}}{\epsilon_m}$	0·28	0·26	0·32	0·25	0·36	0·26	0·15	0·21	
13	Average vertical diffusion	$\overline{\kappa_d N^2}$ (cm^2 s^{-3} $\times 10^3$)	1·1	2·5	*	1·9	5·2	2·0	2·8	16·3	
14		$\frac{\overline{\kappa_d N^2}}{\epsilon_M}$	0·41	0·21	*	0·16	0·30	0·24	0·11	0·25	Average (sample standard deviation) 0·240 (0·097)
15	Minimum gradient Richardson number	R_i	0·44	0·19	0·089	0·068	0·34	0·61	0·59	0·23	
16		$\frac{\nu N^2}{\epsilon}$	0·34	0·19	0·32	0·22	0·11	0·24	0·14	0·07	
17	Turbulent Prandtl number	$\sigma_T = \frac{\nu_i}{\kappa_d}$	48·5	36·7	*	27·1	28·1	36·5	76·5	16·5	
18	Kolmogorov subscale	$(\nu^3/\sigma_T \epsilon_M)^{\frac{1}{4}}$ (cm)	0·054	0·040	*	0·043	0·039	0·044	0·027	0·032	
19	Buoyancy subscale	$(\epsilon_M \sigma_T / N^3)^{\frac{1}{2}}$ (cm)	0·27	0·51	*	0·42	0·56	0·51	1·36	1·17	

* Faulty record

TABLE 1

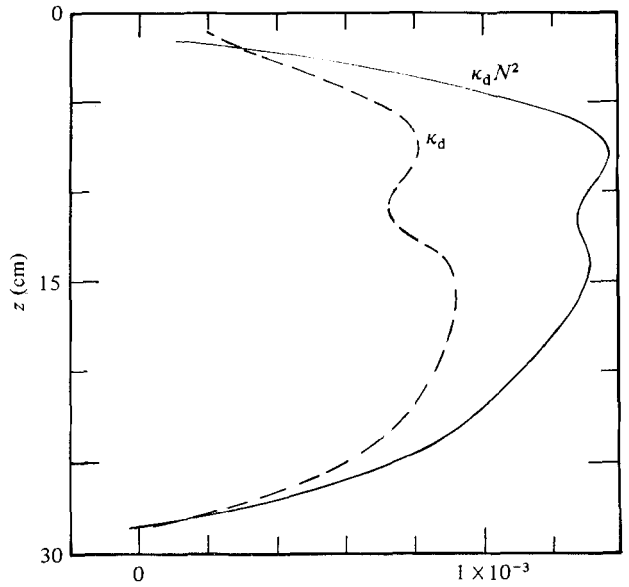

FIGURE 4. Vertical diffusivity as a function of depth z below the upper surface. These profiles are for the run† in table 1. – – –, κ_d (cm^2 s^{-1}); ——, $\kappa_d N^2$ (cm^2 s^{-3}).

Attention is drawn to the difference between this and the expression by Lilley *et al.* (1974) and others, which give a proportionality constant on the right-hand side of $R_f/(1-R_f)$, or, overlooking viscous losses on large scales, $\eta/(1-\eta)$. The expressions are in fact equivalent, since ϵ_M includes both the work done against gravity and the ultimate dissipation against friction on the mixing scales. ϵ_M is therefore larger than the terminal dissipation rate by the factor $(1-\eta)^{-1}$. Nevertheless (9) seems to be a more useful formulation since once mixing scales are reached viscous dissipation is inseparable from ϵ_M.

An inspection of rows (12) and (14) of table 1 confirms (9) even better than might be expected, since mixing was not primarily shear generated. The average value of $\overline{\kappa_d N^2/\epsilon_M}$ is 0·24, equal to the average η to well within the limits of experimental uncertainty but beyond the value of 0·35 to be expected if a factor $\eta/(1-\eta)$ were to apply.

6.3. *Prandtl-number dependence*

Although viscosity and Prandtl number (0·01 cm^2 s^{-1} and 900 respectively) were effectively constant in these experiments, some useful indication of their possible influence on mixing emerges from the results.

In all experiments N^2 was about 1·0 s^{-2}. Therefore from row 13 of table 1 the effective vertical diffusivity of density κ_d was usually much less than the laminar viscosity, although considerably greater than the molecular diffusivity of density κ_s. Nevertheless the 'effective internal viscosity' ν_i (row 10) was usually several times the laminar viscosity, so that the 'turbulent Prandtl number' $\sigma_T = \nu_i/\kappa_d$ was between 16 and 80 (row 17, table 1), considerably greater than unity. In no conventional sense therefore could the field be regarded as 'fully turbulent'.

Richardson's (1920) original argument proposes that the flux Richardson number (or more appropriately here the mixing efficiency η) should equal the mean gradient Richardson number $\overline{R}_i$ divided by the turbulent Prandtl number σ_T. An extension of the argument to the present circumstances might require a dynamical parameter

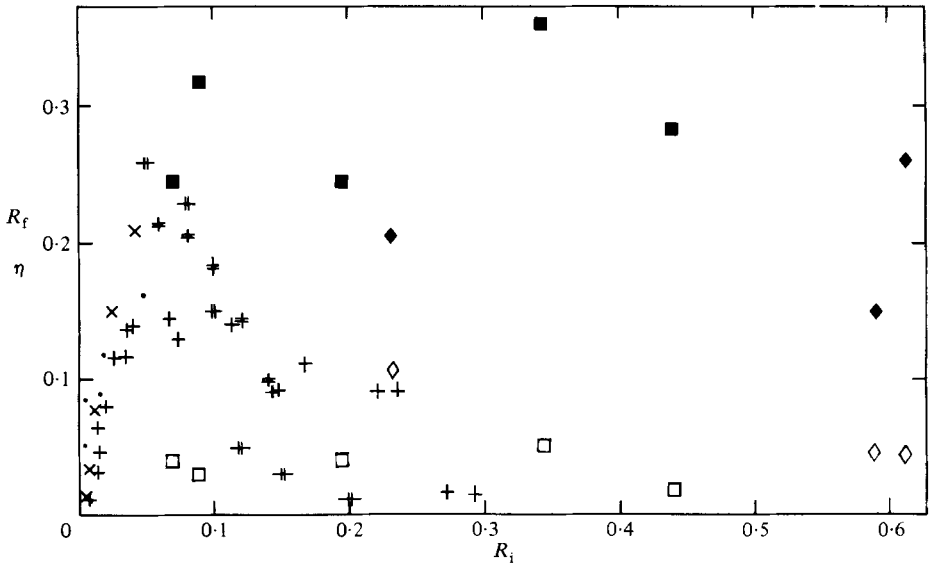

FIGURE 5. Flux Richardson number R_f ($= \dot{p}/\epsilon$ in the present experiments) and mixing efficiency η ($= \dot{p}/\epsilon_M$) versus gradient Richardson number R_i. Open symbols: R_f, present experiments; closed symbols: η, present experiments; crosses and dots: R_f estimate from previous experiments, compiled by Linden (1979).

different from $\bar{R}_i$ but equivalent in its expression of the ratio of buoyant and kinetic energy; any such parameter would be expected to vary inversely with the forcing rate.

However, a comparison of the values in rows 12 and 17 shows that to fit the Richardson relation not only would $\bar{R}_i$ or its equivalent need to be large, but also erratic. *A more plausible conclusion is that η is only weakly dependent on σ_T.*

This is not too difficult to explain in the light of the detailed kinematic observations in McEwan (1983), to which the reader is referred to accompany the following discussion.

Once breaking has occurred and interleaving density microstructure has been created, it is effectively frozen into the field on scales smaller than $O(\delta)$, where $\delta = (\nu/N)^{\frac{1}{2}}$, at which scale viscosity inhibits buoyant untangling. Kinetic energy transferred to such scales during a mixing event is irreversibly lost to viscosity or into buoyancy redistribution. If the extent of an interleaving structure is l the untangling time will be $O(l/q')$, where q' is the velocity scale for the relative interleaving motion.

If Δ is the vertical extent of the mixing event the buoyancy body force per unit mass between interleaving fluid layers will not exceed ΔN^2, and when flattened nearly horizontal through gravitation of the mixing region the horizontal component will be $O(\delta \Delta N^2 l^{-1})$. Equating this to viscous force $O(\nu q'/\delta^2)$ gives $q' = O(\delta^3 \Delta N^2 \nu^{-1} l^{-1})$ or $t = O(\nu l^2 N^{-2} \delta^{-3} \Delta^{-1})$.

For the mixing to be irreversible, significant molecular diffusion of density must occur during this timescale; hence $t > O(\delta^2/\kappa_s)$, and with rearrangement and substitution

$$\frac{\nu}{\kappa_s} = \sigma < O\left(\frac{l}{\delta}\frac{l}{\Delta}\right).$$

l/δ is evidently large in observable cases and l/Δ is at least of order unity. Therefore

unless the Prandtl number for buoyancy is similarly large the mixing efficiency is likely to be insensitive to that number.

The same arguments will not hold for Prandtl numbers appreciably less than unity for in that case diffusion would be complete before relative motion in the mixing region had subsided. Mixing efficiencies might then be greater than those measured here.

6.4. *Application to the ocean and the atmosphere*

Internally induced mixing in the oceans is evidently very intermittent, with actively turbulent regions usually occupying only a small fraction of the volume at any particular time. Woods (1980), assuming this intermittency to be 0·05 such that an appropriate dissipation ϵ_b in the mixing events is twenty times the average internal dissipation, then deduced that the Kolmogorov subscale $(\nu^3/\epsilon_b)^{\frac{1}{4}}$ would be about 3 mm and the buoyancy subscale $(\epsilon_b/N^3)^{\frac{1}{2}}$ about 10 cm. This happens to agree with his observations of the scale of Kelvin–Helmholtz billowing overturn.

Lilley *et al.* (1974) provide data for clear-air turbulence over mountains, clearly identified with internally generated stratified mixing. From this a representative dissipation rate of 20 $cm^2\ s^{-3}$ and N^2 of $4{\cdot}610^{-4}\ s^{-2}$ and a kinematic viscosity of 0·095 $cm^2\ s^{-1}$ yield Kolmogorov and buoyancy subscales of 0·08 and 1420 cm respectively.

In the present experiments, supposing that within *active mixing* regions the turbulent Prandtl number is order unity, then to first approximation the intermittency will be of order the reciprocal of the net turbulent Prandtl number σ_T. Therefore, scaling the mixing dissipation by a factor σ_T the Kolmogorov subscale (table 1, row 18) is about 0·04 cm and the buoyancy subscale (row 19) ranges between 0·3 and 1·4 cm. The scale separation and the intermittency are both roughly comparable to those prevailing in the upper ocean, and the present results should be directly applicable.

In the atmosphere the scale separation is considerably wider, implying a substantial scale cascade beyond breaking before dissipation scales are reached. Together with the low Prandtl number in air this would imply a more complete annihilation of density contrasts in a single event. The effect on net mixing efficiency is hard to gauge because a smaller proportion of the total kinetic energy input is expended before the contrasts are destroyed, leaving a larger residual to be lost to viscosity without further work against gravity. The present results must therefore be regarded cautiously for atmospheric applications.

These experiments could not have succeeded without the ingenuity and perseverance of Mr Ian Helmond, whose contribution is gratefully acknowledged. The apparatus required precise and painstaking construction and this was done by Mr G. Scott and Mr T. Firestone. Mr R. Bell undertook the diffusion integrations. All the work was performed at the CSIRO Division of Atmospheric Physics, Aspendale.

Appendix. Dissipation and energy-partition equations

A 1. *Field description*

The field is taken as an ensemble of linear wave modes satisfying tangentiality on the rectangular boundaries $x = 0, l$; $z = 0, h$ of the container, viz

$$\psi = \Sigma\psi_{j(K,M)} = \sum_K \sum_M A_j \sin\frac{K\pi x}{l} \sin\frac{M\pi z}{h} \sin\omega_j t. \tag{A 1}$$

Owing to imperfections in the linear density profile, the functional dependence on z is an approximation, adopted for convenience in formulating and computing energy, dissipation and interaction coefficients. It is not, however, acceptable in determining the natural frequency of component modes. For this purpose a ray closure integration based upon the WKB approximation was adopted. With $N^2(z) = -(d\rho/dz)\, g^*/\rho$, where $\rho(z)$ is the measured static density profile fitted by a fifth- or sixth-order polynomial, iterations on g^* representing a scaling correction to N were first made to satisfy

$$\int_0^h \left(\frac{N^2(z)}{\omega^2 - 1}\right)^{\frac{1}{2}} dz = \frac{Ml}{K} \tag{A 2}$$

for the fundamental mode $M = K = 1$ using the measured wave frequency ω_a. In regions where $\omega_a^2 > N^2$, N was taken equal to ω. Successive iterations in ω were made using (A 2) for each mode considered using the derived $N(z)$ function.

A 2. *Interaction expressions*

Energy can be lost by internal wave mode 'a' into parasitic lower frequency modes 'b' and 'c' if the triad resonance conditions

$$|\omega_a| - |\omega_b| - |\omega_c| = 0, \tag{A 3}$$

$$\boldsymbol{\kappa}_a + \boldsymbol{\kappa}_b + \boldsymbol{\kappa}_c = 0 \tag{A 4}$$

are approximately satisfied. In the present case with fields defined by (A 1), satisfaction of (A 4) is ensured for approximate modal numbers, but for a given mode 'a' exact resonance is confined to a continuum of interaction pairs which may not include any of these, but which lie on a resonant locus L. The situation in wavenumber space is shown in figure 6. k_j and m_j are horizontal and vertical wavenumbers respectively.

Provided that pairs b, c can be found, and each of b, c are in turn susceptible to destabilization by d, e and f, g respectively, the interaction equations can be written, to lowest order,

$$\left.\begin{aligned}
&\dot{A}_a = F_a - R_a A_a + S_{bc} A_b A_c \quad \text{primary mode;}\\
&\left.\begin{aligned}
\dot{A}_b &= -R_b A_b + S_{ac} A_a A_c + S_{de} A_d A_e,\\
\dot{A}_c &= -R_c A_c + S_{ab} A_a A_b + S_{fg} A_f A_g
\end{aligned}\right\} \text{secondary modes;}\\
&\left.\begin{aligned}
\dot{A}_d &= -R_d A_d + S_{be} A_b A_e,\\
\dot{A}_e &= -R_e A_e + S_{bd} A_b A_d,\\
\dot{A}_f &= -R_f A_f + S_{cg} A_c A_g,\\
\dot{A}_g &= -R_g A_g + S_{cf} A_c A_f
\end{aligned}\right\} \text{tertiary modes.}
\end{aligned}\right\} \tag{A 5}$$

Rs and Ss are net damping and interaction coefficients given by (A 9), (A 10) respectively. Limit solutions are found by setting the $\dot{A}$s to zero; modes a, b and c are susceptible to instability if their amplitudes exceed critical values, respectively

$$\bar{A}_a = \left(\frac{R_b R_c}{S_{ac} S_{ab}}\right)^{\frac{1}{2}}, \tag{A 6a}$$

$$\bar{A}_b = \left(\frac{R_d R_e}{S_{be} S_{bd}}\right)^{\frac{1}{2}}, \tag{A 6b}$$

$$\bar{A}_c = \left(\frac{R_f R_g}{S_{cg} S_{cf}}\right)^{\frac{1}{2}}, \tag{A 6c}$$

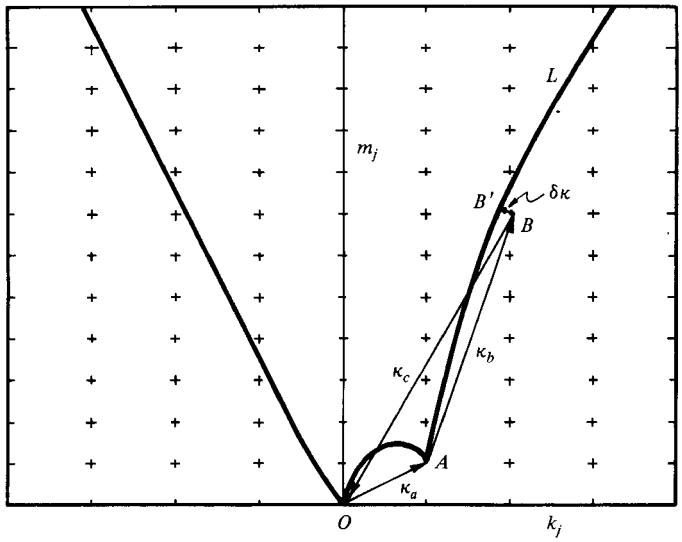

FIGURE 6. Detuned interaction in wavenumber space. The resonant locus L for wavemode 'a' is detuned by $\delta\kappa$ from the nearest triad with integer wavenumbers occupying the rectangular experimental volume.

then, if F_a exceeds $R_a \bar{A}_a$, the terminal amplitude of the parasitic modes is defined; for example for $A_b < \bar{A}_b$, $A_c < \bar{A}_c$

$$A_b = \left[-(F_a - R_a A_{ac}) \left(\frac{S_{ac} R_c}{S_{ab} R_b} \right)^{\frac{1}{2}} S_{bc}^{-1} \right]^{\frac{1}{2}},$$

$$A_c = A_b \left(\frac{S_{ab} R_b}{S_{ac} R_c} \right)^{\frac{1}{2}},$$

$$A_d = A_e = A_f = A_g = 0.$$

If the above gives $A_b > \bar{A}_b$, $A_c < \bar{A}_c$

$$A_b = \bar{A}_b, \quad A_c = A_b \left(\frac{S_{ab} R_b}{S_{ac} R_c} \right)^{\frac{1}{2}},$$

$$A_d = \left[(S_{ac} A_a A_c - R_b A_{bc}) \left(\frac{S_{be} R_e}{S_{bd} R_d} \right)^{\frac{1}{2}} S_{de}^{-1} \right]^{\frac{1}{2}},$$

$$A_e = A_d \left(\frac{S_{bd} R_d}{S_{be} R_e} \right)^{\frac{1}{2}}, \quad A_f = A_g = 0,$$

etc.

A 3. *Detuning*

If several modes sharing triad interaction with the highest-frequency mode j are simultaneously present, the system evolves so that ultimately the only ones remaining are those that yield the lowest $\bar{A}_j$ (McEwan *et al.* 1972). This is useful for defining which parasitic modes are most likely to appear. However, when the system is bounded, there are usually no low-order modes that are precisely resonant, and the calculation of the $\bar{A}_j$ must be modified accordingly.

In wavenumber space (figure 6) detuning is represented by the displacement of grid

intersections representing internal modes from the resonant locus L. For each triad there is a minimum wavenumber difference $\delta\boldsymbol{\kappa}$ represented to near approximation by the shortest path to L. The nearest resonant triad is then represented by the triangle OAB' on the figure.

McEwan & Plumb (1977) showed that detuning increases the critical amplitude $\overline{A}_a$ by a factor

$$\phi_a = [1+|\mathbf{C}_b-\mathbf{C}_c)\,\delta\boldsymbol{\kappa}|^2\,(R_b+R_c)^{-2}]^{\frac{1}{2}}, \tag{A 7}$$

where $\mathbf{C}_b$ and $\mathbf{C}_c$ are group velocities of the resonant partners, regarded as equal and opposite travelling waves, i.e.

$$\mathbf{C}_j = \frac{\omega_j m_j}{|\kappa_j^2|}\left(\frac{m_j}{k_j}, -1\right), \tag{A 8}$$

Of the many possible modes near resonance, the ones selected thus depend critically on the amount of detuning, and their own properties.

A 4. *Interaction and damping coefficients*

The expressions used were adapted from McEwan (1971). Wavenumbers and frequencies were those appropriate to the nearest resonant triads, as defined above and denoted by primes: thus the interaction coefficients are

$$S_{bc} = \left(\frac{k_a'}{\omega_a'} + \frac{k_b'}{\omega_b'} + \frac{k_e'}{\omega_c'}\right)\overline{(k_b'\omega_c' - k_c'\omega_b')\,(k_c'm_b' - k_b'm_b')\,(16\omega_a'\omega_b'\omega_c')^{-1}}. \tag{A 9}$$

S_{ab} and S_{ac} and coefficients for *bde* and *cfg* interaction are given by substitution with subscripts in cyclic order.

Damping is assumed to be given by dissipation due to laminar friction in Stokes-type wall boundary layers on all sides, plus an internal pseudo-viscous dissipation with an adjustable internal viscosity ν_i. With the motion field approximated by the linear inviscid wavefield, the dissipation coefficient is then

$$R_j = \frac{\omega_j\,[hlm_j'(m_j'+k_j') + 2whk_j'\,m_j' + 2wlm_j'^2]\,h}{|\kappa_j|^2\,(2R_{ej})^{\frac{1}{2}}} + \frac{\nu_i h^2\omega|\kappa|^2}{2\omega h^2}, \tag{A 10}$$

where w is the chamber width and $R_{ej} = \omega_j h^2/\nu$ is the Stokes number.

For the fundamental mode only, an additional constant was added to account for measured losses due to leakage past the paddle.

REFERENCES

Gargett, A. E. 1976 An investigation of the occurrence of oceanic turbulence with respect to finestructure. *J. Phys. Oceanogr.* **6**, 139–156.

Gregg, M. & Briscoe, M. G. 1979 Internal waves, finestructure, microstructure and mixing in the ocean. *Rev. Geophys. Space Phys.* **17**, 1524–1528.

Koop, C. G. 1976 Instability and turbulence in a stratified shear layer. Ph.D. dissertation, University of Southern California.

Lilley, D. K., Waco, D. E. & Adelfang, S. I. 1974 Stratospheric mixing estimated from high-altitude turbulence measurements. *J. Appl. Met.* **13**, 488–493.

Linden, P. F. 1979 Mixing in stratified fluids. *Geophys. Astrophys. Fluid Dyn.* **13**, 3–23.

McEwan, A. D. 1971 Degeneration of resonantly-excited standing internal gravity waves. *J. Fluid Mech.* **50**, 431–448.

McEwan, A. D. 1983 The kinematics of stratified mixing through internal wavebreaking. *J. Fluid Mech.* **128**, 47–57.

McEwan, A. D., Mander, D. W. & Smith, R. K. 1972 Forced resonant second-order interaction between clamped internal waves. *J. Fluid Mech.* **55**, 589–608.

McEwan, A. D. & Plumb, R. A. 1977 Off-resonant amplification of finite internal wave packets. *Dyn. Oceans Atmos.* **2**, 83–105.

McEwan, A. D. & Robinson, R. M. 1975 Parametric instability of internal gravity waves. *J. Fluid Mech.* **67**, 667–687.

Olbers, D. J. 1976 The internal wave field in the deep ocean. *J. Fluid Mech.* **74**, 375–399.

Richardson, L. F. 1920 The supply of energy from and to atmospheric eddies. *Proc. R. Soc. Lond.* A **97**, 354–373.

Thompson, R. O. R. Y. 1980 Efficiency of conversion of kinetic energy to potential energy by a breaking internal gravity wave. *J. Geophys. Res.* **85**, 6631–6635.

Thorpe, S. A. 1973 Experiments on instability and turbulence in a stratified shear flow. *J. Fluid Mech.* **61**, 731–751.

Turner, J. S. 1973 *Buoyancy Effects in Fluids.* Cambridge University Press.

Weinstock, J. 1978 Vertical turbulent diffusion in a stably stratified fluid. *J. Atmos. Sci.* **35**, 1022–1027.

Woods, J. D. 1980 Do waves limit turbulent diffusion in the ocean? *Nature* **288**, 219–224.